ORIGINAL RESEARCH

Numerical simulation of friction extrusion: process characteristics and material deformation due to friction

George Diyoke[1] · Lars Rath[1] · Rupesh Chafle[1] · Noomane Ben Khalifa[1,2] · Benjamin Klusemann[1,2]

Abstract

This study employs a finite element thermo-mechanical model, using a Lagrangian incremental setting to investigate friction extrusion (FE) under varying process conditions. The incorporation of rotation in FE generates substantial frictional heat, leading to significantly reduced process forces in comparison to conventional extrusion (CE). The model reveals the interplay between temperature, strain, and strain rate across different microstructural zones of the resulting wire. Specifically, the sticking friction condition in FE enhances initial shear deformation, aligning with a homogeneous spatial strain distribution and predicting complete grain refinement in the extruded wire, as per Zener-Hollomon calculations. On the other hand, under the sliding friction condition in FE, the shear deformation is reduced which results in an inhomogeneous microstructure in the extruded wire. The analysis of material flow in the workpiece reveals distinct transitions from the base material to the thermo-mechanically affected zones. The simulated process force, thermal history, and microstructure during sliding friction conditions align well with the findings from performed friction extrusion experiments.

Keywords Process simulation · Friction condition · Thermo-mechanical condition · Material flow behavior · Dynamic recrystallization · Microstructure zones

Introduction

In recent times, there has been a notable research interest in friction extrusion (FE) due to its capability to produce extrudates with microstructural refinement, which correlates to improved mechanical properties of extruded wire and rods [1, 2]. In terms of advanced processing techniques, FE can be

✉ George Diyoke
george.diyoke@hereon.de

Lars Rath
lars.rath@hereon.de

Rupesh Chafle
rupesh.chafle@hereon.de

Noomane Ben Khalifa
noomane.ben_khalifa@hereon.de

Benjamin Klusemann
benjamin.klusemann@hereon.de

1   Institute of Material and Process Design, Helmholtz-Zentrum Hereon, Max-Planck-Straße 1, Geesthacht 21502, Germany

2   Institute for Production Technology and Systems, Leuphana University Lüneburg, Universitätsallee 1, Lüneburg 21335, Germany

seen as a paradigm shift from the conventional extrusion (CE) process due to the addition of die rotation. The localized thermo-mechanical conditions created at the process zone in FE contribute towards reducing energy consumption while enhancing crucial mechanical properties, including strength, fatigue resistance, and ductility [3].

The operational principle of FE compared to CE allows for a reduction in the process steps and maintains hot working conditions while processing below melting temperature. This prevents solidification defects such as alloy segregation, shrinkage, or gas porosity [4]. In FE, hot working condition is achieved through relative rotation and translation of the die against the feedstock, leading to heat generation. Since a non-consumable rotating tool is used as a die, the feedstock in the container can be in various conditions, such as chips, powder, or bulk material [5–7]. The friction applied at the die-feedstock interface and die rotation, leads to frictional heating and severe plastic deformation, as feedstocks are extruded to produce rods, wires or tubes [8, 9]. The extruded wires from FE can be used as feedstock materials for additive manufacturing [10]. The prevailing thermo-mechanical condition in FE needs to be explored for a better understanding of the material deformation and flow behavior.

Numerical models are useful to understand and even predict the complex conditions in FE. Finite element method (FEM) has been popular for modeling different friction-based processes due to its ability to capture the macro-mechanical process dynamics [6, 11–13]. Using the FEM simulation package DEFORM, a 3D Lagrangian method coupled with visco-plastic material behavior was implemented to investigate the extrusion of metal chips [6]. Since FE operates on a process mechanism similar to friction stir welding/processing (FSW/P), understanding the principles of FSW/P can provide valuable insights for modeling FE [6]. Numerical modeling of the FSSW process based on the Coupled Eulerian-Lagrangian technique was developed in ABAQUS to investigate the material flow [14]. The modeling and experimental observations provide a consistent interpretation of the circumferential material flow which has some inward radial flow at the top surface. An Arbitrary Lagrangian Eulerian (ALE) formulation implemented in Forge3 was used to study material and interface behavior in FSW [15]. The model used reproduced a temperature profile that agrees with the experiment. The ALE framework within ABAQUS was deployed to model FE in 2D to investigate the metallurgical transformation of magnesium chips [16]. The model framework showcases its remarkable capability to predict the deformation process and its consequential microstructural attributes to grain size and microhardness. However, within the FEM framework, the effects of friction conditions leading to material flow behavior in FE are not fully investigated.

Friction plays a significant role in friction-based processes, and its accurate representation is essential for obtaining realistic material flow simulation results. The commonly adopted friction models which captures the friction conditions in FEM are Shear and Coulomb friction models. The Shear friction model has been used to model material flow in FSW [17]. But also Coulomb friction model with temperature-dependent friction coefficient has been used, for instance, to simulate refill FSSW [13], which led to accurate process prediction of thermal history in refill FSSW. In FEM, applying an adaptive mesh in the Lagrangian domain at the contact region enhances the resolution of the nonlinear friction condition between the die and the feedstock without increasing the computational demand [6, 18]. The interplay between frictional heat generation and (temperature-dependent) material response to deformation establishes a crucial connection between the friction conditions and the material model within the FEM.

The numerical models have shed light on the influence of contact conditions on thermo-mechanical features to some extent. However, a comprehensive understanding of the friction conditions leading to shear deformation, material flow against the die-face and the formation of microstructural zones in the extruded wire is still an under-explored domain

in FE. The main aim of this work is to understand the relationship between applied friction conditions and the resultant thermo-mechanical conditions leading to various microstructural zones during FE. A finite element thermo-mechanical model based on a 3D Lagrangian incremental setting is used. Sticking and sliding friction conditions based on the shear and Coulomb model, respectively are applied in FE to address the deformation mechanism. Furthermore, CE is simulated as well to understand the significance of rotation in FE.

This work is organized as follows: the model description comprising of the experimental setup, process model, material, heat, and friction conditions are presented in "Model description". In "Results and discussion", numerical validation with experiments and other results are discussed. "Conclusion" enlists the key conclusions of the study.

Model description

The setup of the experiment is elucidated in "Experimental setup". The process geometries with mesh specifications are illustrated in "Process model". In "Material response, heat generation, and friction conditions", the constitutive model and heat generation as well as the friction conditions are discussed. In the final subsection "Process simulation input parameters", simulation inputs corresponding to the FE experiment, literature-deduced values, and applied thermal conditions are reported.

Experimental setup

FE was performed using the FE100 (Bond Technologies, IN, USA), a dedicated FE machine, where a detailed illustration can be found in [19]. The tooling setup consists of a rotating 42CrMo4 steel container of 50 mm inner diameter and X40CrMoV5-1 flat die (90° die angle edge) with a 14 mm bore, leading to an extrusion ratio of 12.76. In addition, a constant force of 300 kN and spindle rotation at 90 rpm were applied during the process. The die position, temperature, and spindle torque were measured. The temperature was recorded via a K-type thermocouple at two-third of the die radius within the die, located 1 mm from the die face. The feedstock material AA7075 in as-cast condition was machined to 50 mm length and 49.50 mm diameter and locked against rotation towards the container. To start the FE process, a program step with higher rotation and lower force (300 rpm, 50 kN) was used to ensure a defined contact between the die and feedstock, thereby avoiding torque overload.

For microstructural analysis, the samples underwent standard metallographic sample preparation, involving sectioning, grinding, and polishing with 0.25 μm colloidal silica-suspension. Subsequently, electro-polishing for 90 s at 20 V with Barker's reagent was performed. The microstructures
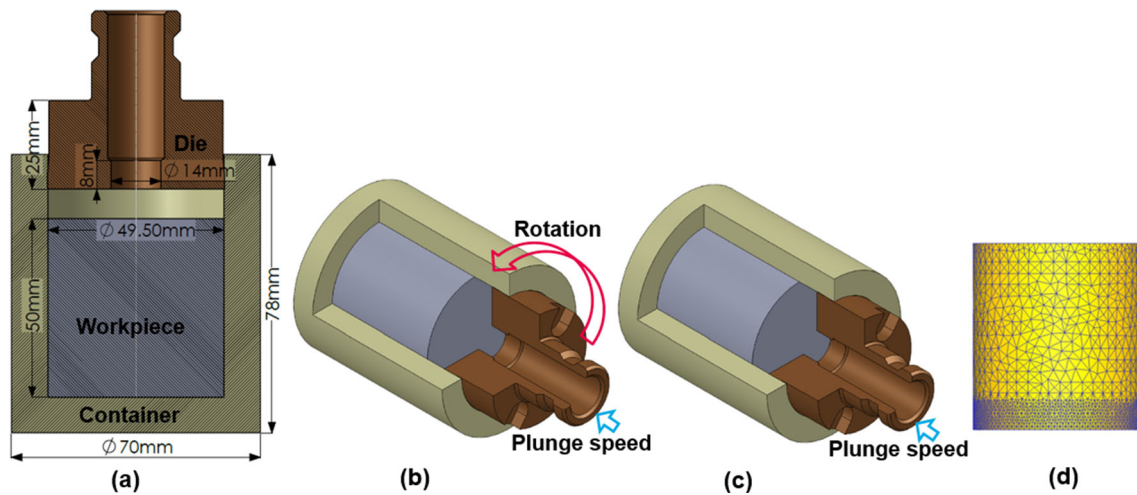
Fig. 1 Schematic of (a) FE and CE setup illustrating dimensions; (b) FE setup depicting die rotation and translation (c) CE setup showing die translation; and (d) workpiece showing Lagrangian domain with mesh density

were then examined and results captured using a Keyence VHX-600 digital microscope with polarized light.

A detailed microstructural analysis was conducted using an FEI Quanta 650 field emission gun scanning electron microscope (SEM). The instrument is outfitted with a TSL OIM electron backscatter diffraction (EBSD) system and an EDAX energy dispersive X-ray spectroscopy (EDS) system. The EBSD analyses were performed for characteristic microstructral zones via a step size of 0.2 μm at a voltage of 15 kV.

Process model

The simulation setup in DEFORM 3D for both CE and FE processes have the same object dimensions as shown in Fig. 1(a). The illustration in Fig. 1(b) and (c) shows the applied die rotation[1] and translation w.r.t. workpiece in FE and die translation without rotation in CE, respectively. The boundary conditions are applied in terms of velocities. The cylindrical workpiece, measuring 49.50 mm × 50 mm, is discretized using a mesh of around 50,000 tetrahedral elements of variable size, as shown in Fig. 1(d). The variable element size aids in re-meshing steps and forms a mesh density window at one end of the workpiece, which is in contact with the die. The re-meshing steps based on the ratio of penetration distance of the die in the element is set to 0.7. Hence, at the contact region, the re-meshing step ensures a higher quality of the new mesh by conserving the calculated thermo-mechanical state of the workpiece during simulation [20]. The refined mesh density follows the die movement, and the size is about 10 times smaller than the largest mesh size

in the workpiece. Although the extrusion die and container are modeled as rigid bodies, heat transfer is considered to account for the thermal properties of H13 steel. Therefore, the extrusion die and the container are meshed using 20,000 tetrahedral elements.

Material response, heat generation, and friction conditions

The workpiece material used is AA7075, which is modelled as rigid visco-plastic. A hyperbolic-sine constitutive equation based on an Arrhenius-type relationship is applied to predict the flow stress as follows,

$$\dot{\bar{\varepsilon}} = A\big[\sinh(\alpha\bar{\sigma})\big]^n \exp\Big(-\frac{\Delta H}{RT}\Big), \qquad (1)$$

where $\dot{\bar{\varepsilon}}$ is the strain rate, $\bar{\sigma}$ is the flow stress, ΔH is the activation energy, R is the universal gas constant, T is the absolute temperature, and A, n and α are material constants [21, 22].

The contribution of friction and plastic deformation, at the workpiece-die interface in FE is simplified as $\dot{q} = \dot{q}_f + \dot{q}_p$ where $\dot{q}$ is the rate of total heat generated during the process, $\dot{q}_f$ is the rate of frictional heat generated, and $\dot{q}_p$ is the rate of heat generated due to plastic deformation of the material. In DEFORM 3D, the expression of heat generation due to plastic deformation which incorporates the inelastic heat fraction reads [18] $\dot{q}_p = \eta\bar{\sigma} \times \dot{\bar{\varepsilon}}$ where η is the inelastic heat fraction or amount of mechanical work converted to heat.

The Coulomb friction model is applied to capture the sliding between the die and the workpiece, as established by Shen [23]. The sliding friction condition is expressed in terms of contact shear stress as $\tau_{contact} = \mu\tau_{fric} = \mu P$, where P is the contact pressure of a sliding die during rotation, and

---

[1] The die rotation led to the same results as container rotation in the simulation.

the friction coefficient μ is considered to be temperature-dependent in this study. On the other hand, to model the sticking friction condition at the contact region, the Shear friction model is adopted. In this case, the yield strength of the material is the limiting condition of contact shear stress at the interface [18], and expressed as $\tau_{contact} = m\tau_{yield}$, where τ_{yield} is the shear yield strength of the material and m is a shear friction factor.

Process simulation input parameters

Flow stress data of AA7075 alloy is deduced from hot compression tests conducted at deformation temperatures between 300 °C and 500 °C under strain rates of 0.001–10 s^{-1} [24, 25]. The values used in the simulation are provided in Table 1. Figure 2 shows the die velocity-time curve obtained from the force-controlled FE experiment (described in "Experimental setup"), which is used as boundary condition for the die in the FE simulations. The temperature-dependent friction coefficient used for the sliding condition, i.e. Coulomb model is given in Table 2. To ensure comparability with FE, for CE case, a constant plunge speed of 0.35 mm s^{-1} is applied at room temperature; and the other parameters remain the same as FE with sticking condition. The initial temperature of all parts is assumed to be at room temperature, i.e. no preheating is performed.

Results and discussion

The thermo-mechanical process model of FE is first validated with experimental data in "Numerical validation of FE". The influence of die rotation and friction condition on the force
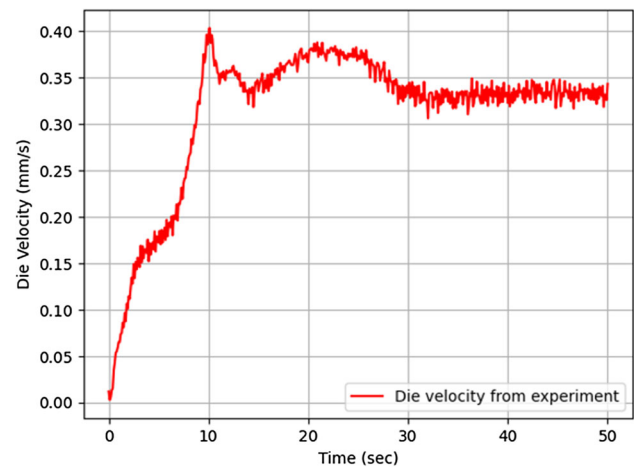
Fig. 2 Evolution of die velocity during the force-controlled FE experiment

and thermal history are reported in "Effect of die rotation and friction conditions on the process history". The description of microstructural zones observed during the FE experiment is presented in "Microstructural zones in the workpiece". The contribution of sticking condition to material deformation and flow is detailed in "Thermo-mechanical conditions and characteristics of sticking friction condition in FE". Finally, in "Material flow and microstructure zones due to sliding friction condition in FE", the resulting microstructure evolution under sliding friction conditions is discussed.

Table 1 Material parameters for AA7075 and further simulation parameters employed in the extrusion process simulations	Parameters	Symbols	Magnitude	Units
	Material constant [24, 25]	A	1.0×10^{9}	s^{-1}
	Material constant [24, 25]	n	5.4	—
	Stress exponent [24, 25]	α	0.014	MPa^{-1}
	Activation energy [24, 25]	ΔH	129	kJ mol^{-1}
	Poisson's ratio of Al [18]	ν^{Al}	0.33	—
	Density of Al	ρ^{Al}	2.67×10^{-6}	kg mm^{-3}
	Thermal conductivity of Al [18]	κ^{Al}	125	N s^{-1} $°C^{-1}$
	Heat convection coefficient [18]	$h^{convection}$	0.02	N s^{-1} mm^{-1} $°C^{-1}$
	Heat conduction coefficient [18]	$h^{conduction}$	11	N s^{-1} mm^{-1} $°C^{-1}$
	Reference temperature	T^{room}	20	°C
	Die rotational speed	ω^{speed}	90	rpm
	Total process time	$t^{process}$	50	s
	Simulation time step	t^{step}	0.4	—
	Shear friction factor [27]	m	0.7	—
	Inelastic heat fraction [28]	η	0.9	—
	Extrusion ratio	ER	12.76	—

Table 2 Coulomb friction coefficient as a function of temperature [26, 29, 30]

μ	0.5	0.5	0.5	0.26	0.2	0.1	0.08
T (°C)	20	160	200	300	400	500	600

Numerical validation of FE

The die force obtained during the process simulation agrees well with the experimental input force of approximately 300 kN as shown in Fig. 3(a). The high peak force in the velocity-controlled simulation of FE can be attributed to the extrusion speed which is the main parameter that is controlled contrary to the force-control in experiment. Furthermore, the temperature-time profile deduced from the location of the thermocouple (TC) (see Fig. 3(b)) on the die is compared with the experimental measurement. The observed result in Fig. 3(b) shows good agreement with the experiment. In conclusion, the process model represents well the process history from the experiment.

Effect of die rotation and friction conditions on the process history

To examine the impact of die rotation, a comparison is presented with the force profiles of both FE and CE. In CE, a higher die force is obtained compared to FE because of the absence of rotation or preheating. The decrease in force in FE also affirms the energy efficiency of the process compared to CE. Furthermore, within FE for different friction conditions i.e sticking and sliding condition, Fig. 4(a), a variation in the initial force history between the two friction conditions is observed.

Figure 4(b) illustrates the predicted force history in FE with sticking friction condition. The force history is catego-rized into two stages, namely: initial shear deformation (stage I) and extrusion (stage II). The main difference between the stages is that in stage I no extrusion is achieved, while stage II marks the onset of extrusion. In stage I, as the extrusion die makes contact with the workpiece, the force increases rapidly. The decrease in force at 0.5 s and increase at 2 s can be referred to an outcome of the initial material shear-ing. After 2 s, the extrusion starts and gradually proceeds to a quasi-steady-state [31–33]. These stages align with the extrusion transient and steady-states, respectively as reported by Baffari et al. [34].

In addition to the force history, the thermal history dur-ing FE for both friction conditions are investigated. For both FE simulations, the temperature increases rapidly at initial contact between the die and the workpiece. The rotation applied in FE results in heat generation at the extrusion die-workpiece interface. As the extrusion progresses, the temperature depicts a gradual increase correlated with the decrease in the force. In the case of sticking conditions dur-ing FE, there is no relative motion between the material and the die, which minimizes frictional heating, resulting in lower heat generation. In sliding friction condition, a higher tem-perature profile but lower force are predicted compared to the sticking case.

Microstructural zones in the workpiece

Figure 5(a) illustrates distinct zones identified in the work-piece after performing the FE experiments. The typical microstructural zones in FE include two thermo-mechanically affected zones (TMAZ 1 and 2) and the base material (BM) [35]. The BM is shown in Fig. 5(b), representing the feedstock material still unaffected by the FE process. TMAZ 2, representing the transition region between BM and TMAZ 1, as shown in Fig. 5(c), experienced significant
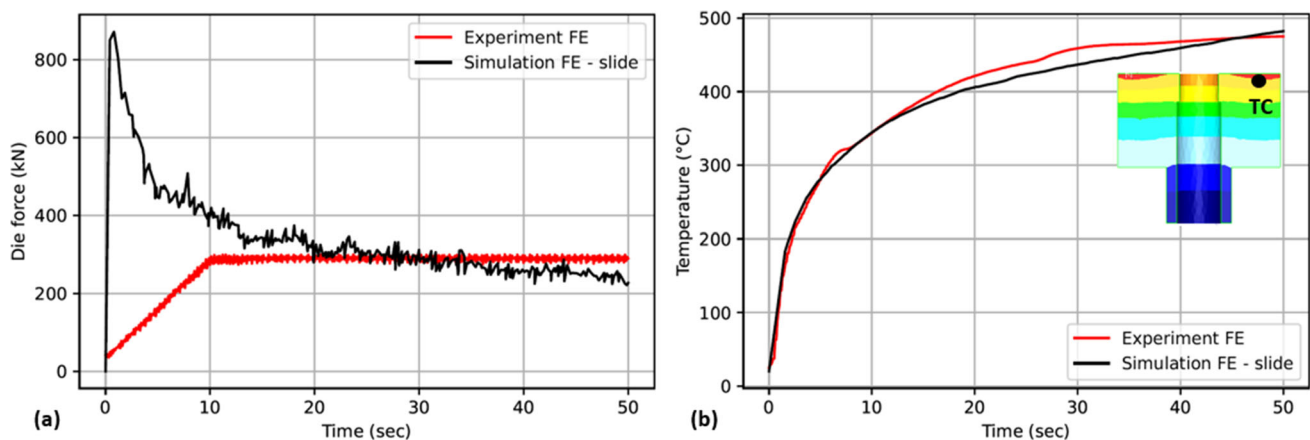
Fig. 3 FE process history validation; (a) force; and (b) thermal history
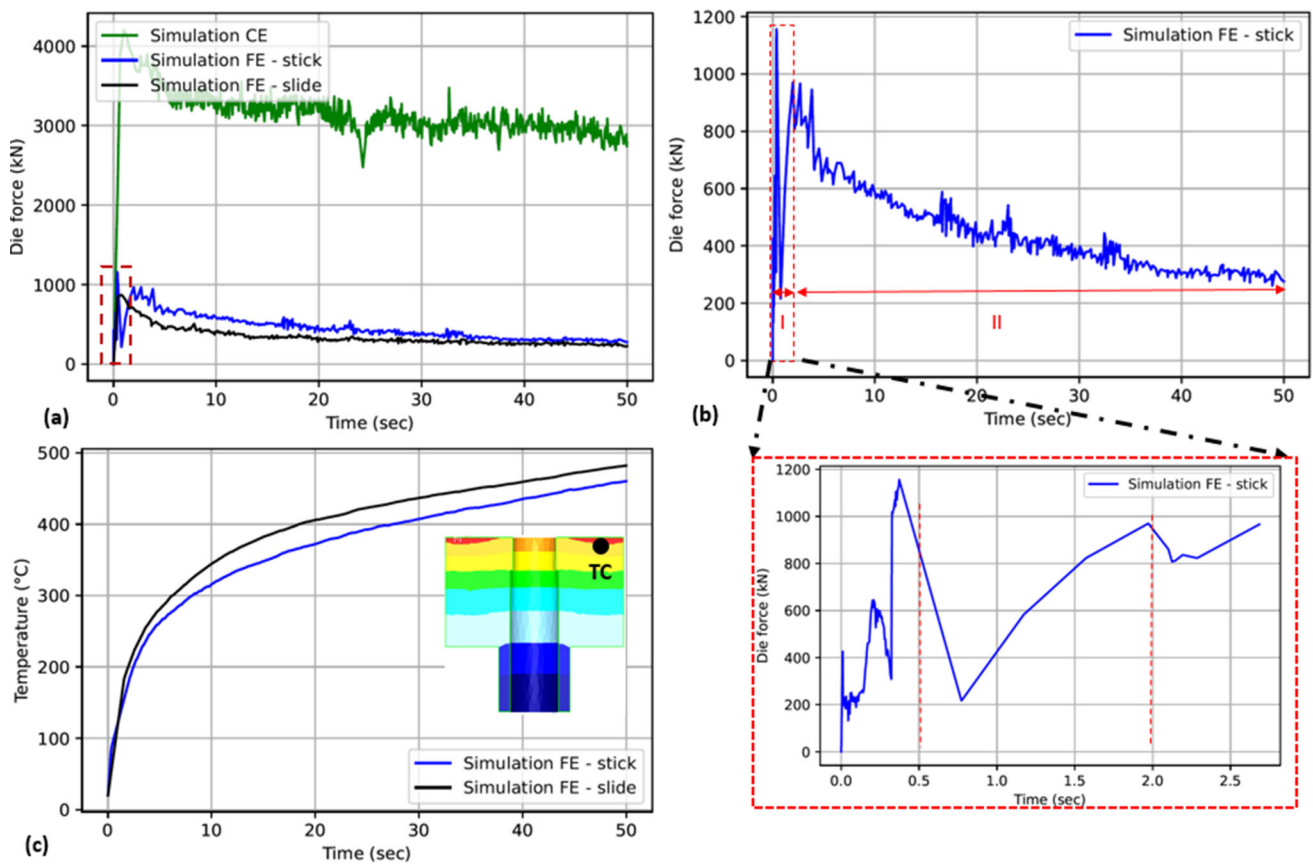
Fig. 4 Process histories: (a) force during CE and FE; (b) force during FE with sticking condition, elucidating deformation stages; and (c) thermal history during FE

temperature and deformation, but not sufficient to induce dynamic recrystallization (DRX). This zone represents also the core part of the wire. However, the main deformed area comprises of the TMAZ 1, which underwent significant plastic deformation at elevated temperature, leading to a fine-grained microstructure, see Fig. 5(d). This zone is mostly already formed in front of the die orifice in the feedstock material as shown via kind-of stop-action experiments by Suhuddin et al. [35]. It has been shown by the authors that for sticking conditions a fully homogenized wire can be achieved due to the introduction of severe shear strains.

Figure 6(a) shows the microstructural zones and the related grain sizes obtained in the experiment. Figure 6(b) depicts grain structures in the BM with considerable alignment in the vertical (ED) direction. The BM consists of coarse and elongated grain. Figure 6(c) shows a tilted grain structure in the TMAZ 2, with grain sizes of 5.38 μm. The grains have mainly undergone deformation but no significant DRX. The TMAZ 1 in Fig. 6(d), depicts a refined grain structure due to DRX, where Suhuddin et al. [35] identified continuous dynamic recrystallization (CDRX) and geometric dynamic recrystallization (GDRX) as the main mechanism with only

limited discontinuous dynamic recrystallization (DDRX). The grain size was determined as 2.56 μm. Understanding the microstructural evolution in these zones is crucial to tailor the mechanical properties of the extruded wire.

Thermo-mechanical conditions and characteristics of sticking friction condition in FE

To reveal the evolution of the initial thermo-mechanical conditions during FE, the material flow velocity maps are shown at three different process times in Fig. 7. Based on these, the in-plane shear evolution on the workpiece due to sticking condition within the initial shear deformation stage (stage I) can be estimated. The radial die velocity is calculated as $v = \omega^{speed} \times r$, where ω^{speed} is rotational speed in radians per second and r is the die radius. Sticking at the interface ensures equal velocity between the die and the workpiece. In Fig. 7(a), initial shearing is observed at 0.05 s around the die orifice with a minimum relative velocity of 65.8 mm s^{-1}. This is followed by an increase in radial velocity distribution affirming continuous material shearing as depicted in Fig. 7(b). After 2 s of processing time, a complete material shearing is
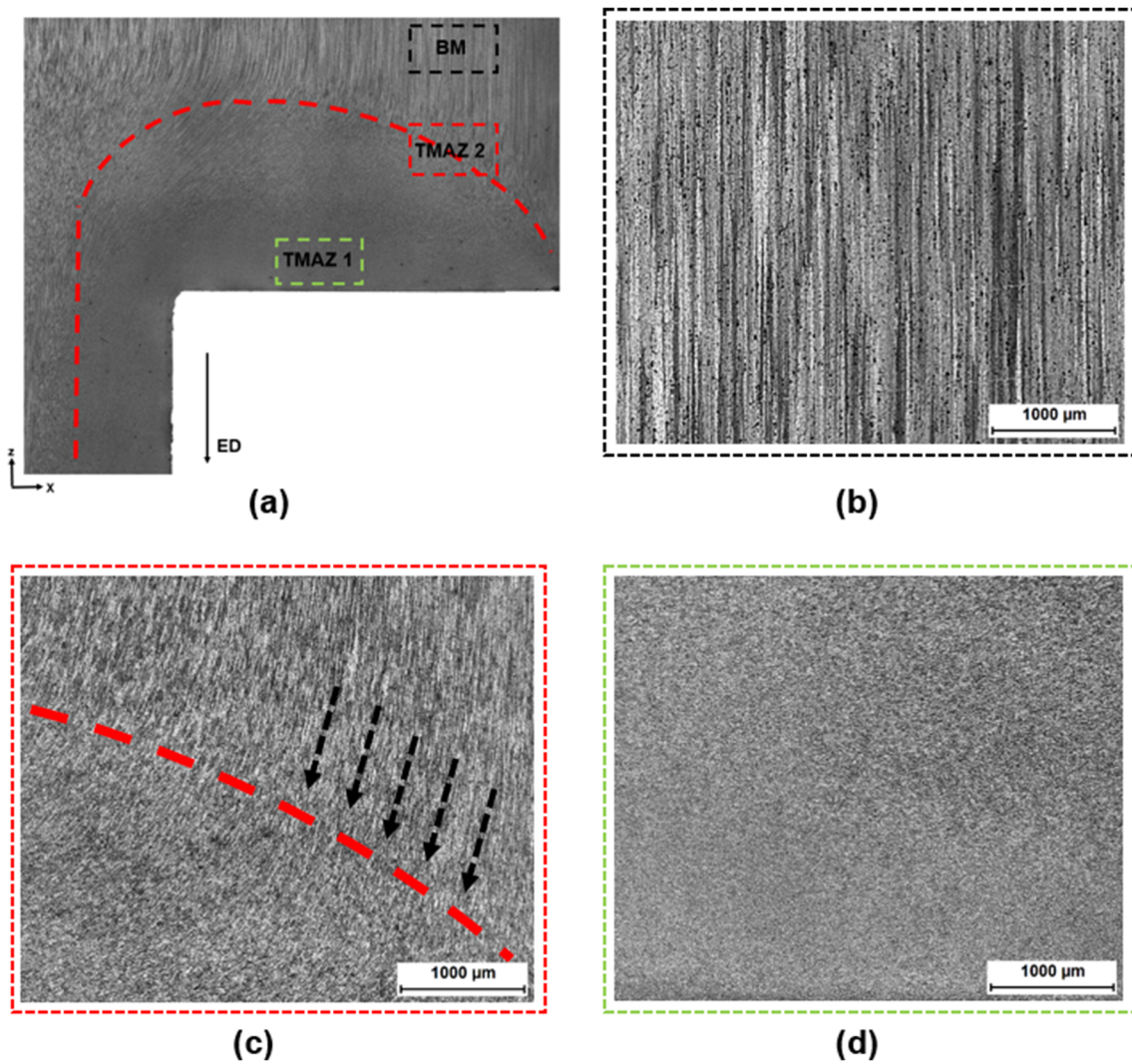
Fig. 5 (a) Micrograph from the FE experiment showing characteristic microstructural zones; (b) BM; (c) TMAZ 2; and (d) TMAZ 1

observed in the workpiece as shown in Fig. 7(c) with a maximum relative velocity of 234 mm s^{-1}. The FE simulation with sticking condition shows that complete material shearing at the contact interface occurs within stage I, corresponding to the illustration in the process history in Fig. 4(b). Following the velocity analysis, the workpiece material sticking to the radial surface of the die rotates at the same velocity as the die. This assertion agrees with the investigation of sticking behavior in SPH model of FE [7] and CFD model of FSW [36]. Figure 8(a-b) illustrates the spatial temperature and strain at 50 s. The maximum temperature is observed at the contact region with the die-face at 478 °C. The strain evolution can be traced and attributed to shear deformation at the contact region. In the extruded wire, strains are redistributed due to rotation leading finally to a homogeneous spatial strain distribution. The contribution of the initial shear deformation and the strain in the extrusion direction assists in the shear plane alignment which characterizes the FE process.

The corresponding microstructure zones i.e. TMAZ 1, 2, and BM, due to sticking condition are depicted in Fig. 8(a-b). The spatial thermo-mechanical distribution results in different degrees of softening across the workpiece and extruded wire in FE. Based on the thermo-mechanical conditions, the grain size evolution is determined through the Zener-Hollomon parameter Z, which is given by the expression, $Z = \dot{\bar{\varepsilon}} \exp(\Delta H / RT)$ [37]. The average grain size (d) is expressed as $d = (a + b \times lnZ)^{-1}$, ($a = -2.44$, $b = 0.1$) for AA7075 as suggested by Cerri et al. [38]. Figure 8(c) and (d) confirm the different regions in the workpiece in terms of the corresponding Z parameters and grain size, respectively. TMAZ 1 in the wire exhibits a high Z value and a small grain size (see Fig. 8(c) and (d)) compared to the other regions in the workpiece, due to the occurrence of DRX driven by the contribution of temperature and strain. The grain size in the TMAZ 1, determined to be around 2 - 3 μm within the wire in the simulation, aligns well with the experimentally calculated

Fig. 6 (a) FE extruded sample with corresponding EBSD maps for different microstructural zones; (b) BM; (c) TMAZ 2; and (d) TMAZ 1
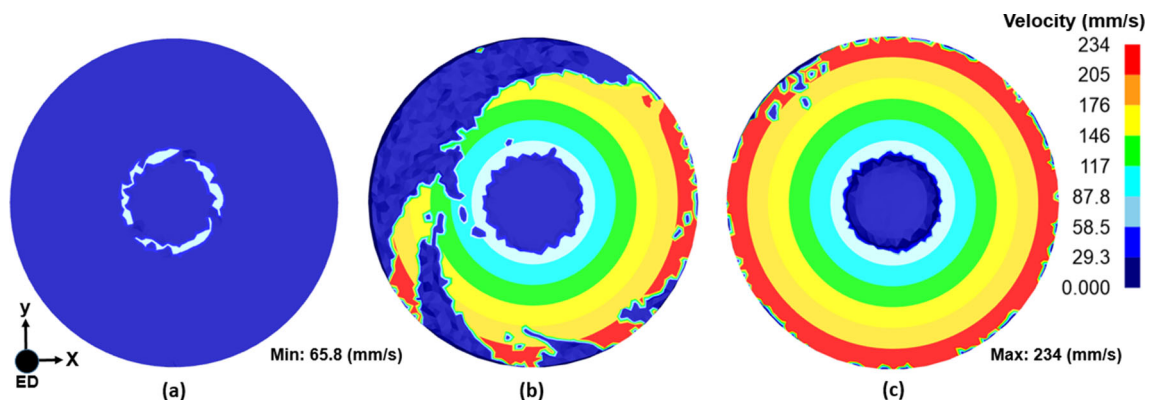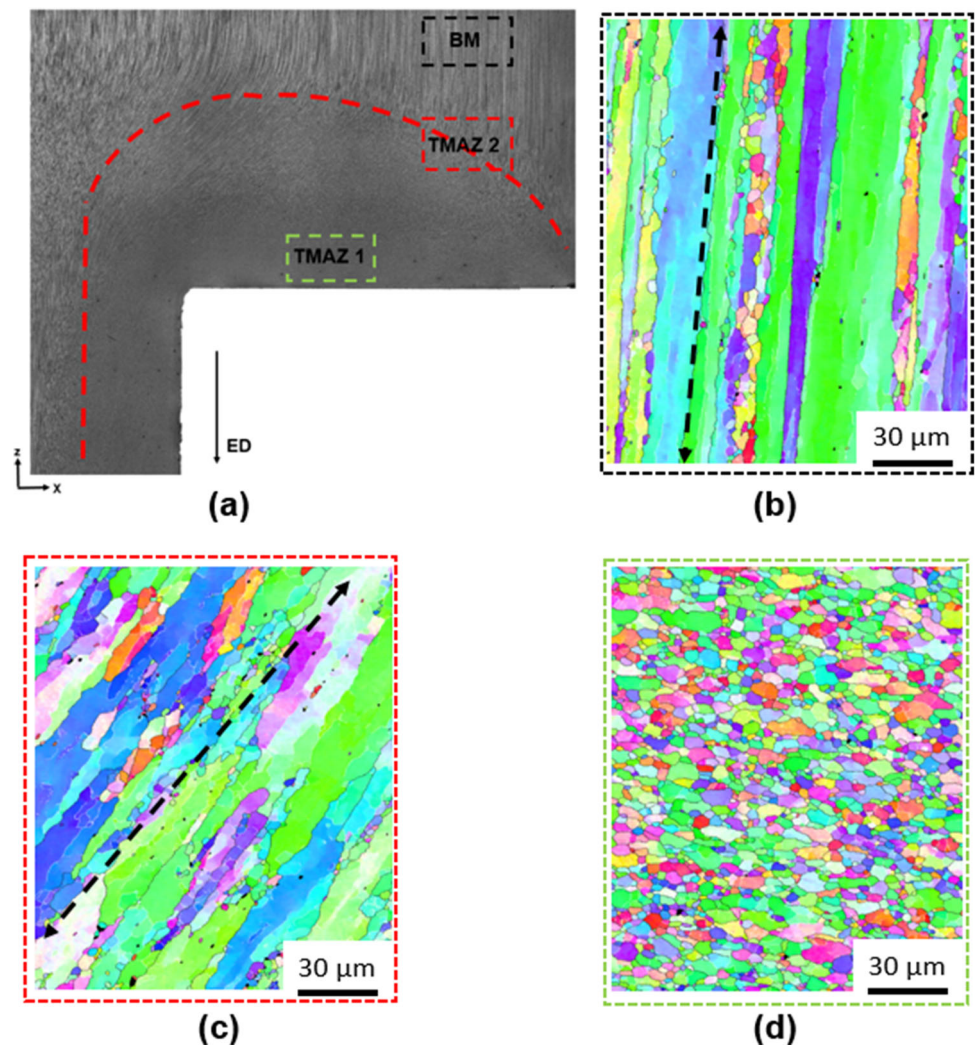
Fig. 7 The velocity maps at the contact region which is perpendicular to the extrusion direction (in-plane) during FE, depicting the evolution of material shearing due to rotation at process time; (a) $t^{process} = 0.05$ s (b) $t^{process} = 0.5$ s; and (c) $t^{process} = 2$ s
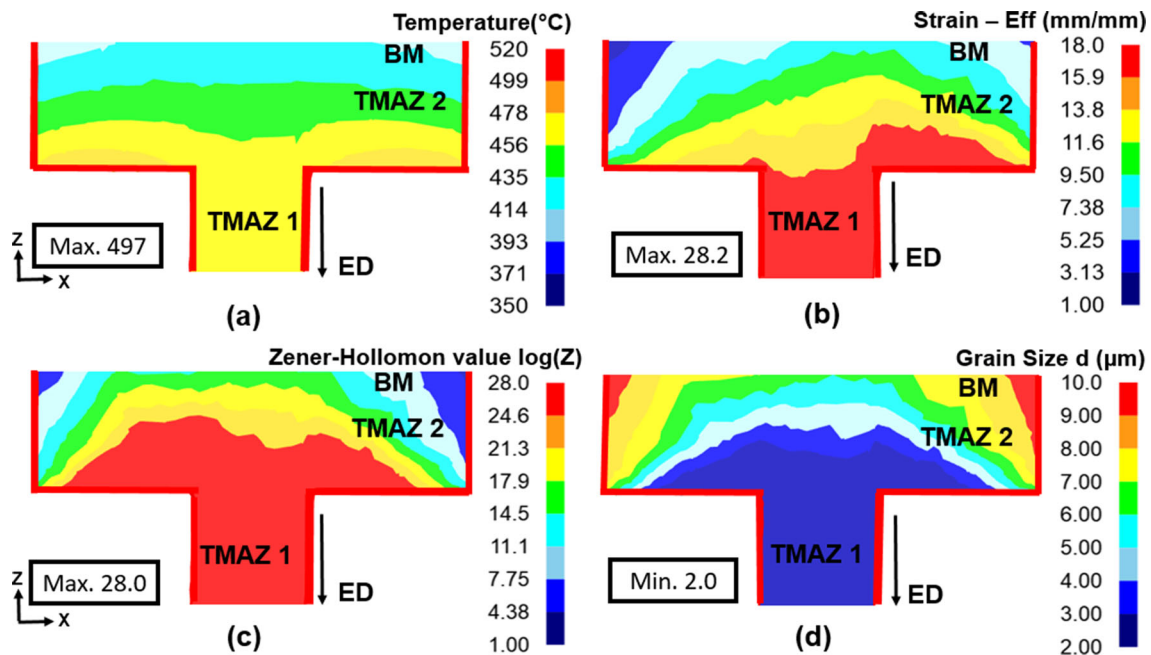
Fig. 8 Spatial distribution of (a) temperature; (b) strain; (c) Zener-Hollomon parameter; and (d) grain size in the workpiece with sticking friction condition applied at the die-workpiece interface in FE at $t^{process}$ = 50 s

of 2.56 μm (see TMAZ 1 in Fig. 6(d)). The occurrence of CDRX was reported in the TMAZ 1 for a fully refined wire. The occurrence of CDRX was reported in the TMAZ 1 for a fully refined wire [35]. As shown in Fig. 8(c), the obtained Z values are below 28.6, which was reported as the transition value from CDRX to DDRX by Sun et al. [39], inferring that CDRX occurs in this case.

This implies that high strain values cause dislocation density to increase and consequently lead to an increase in misorientation. The increase in grain boundary misorientation transforms LAGBs into HAGBs through sub-grain rotation. In TMAZ 1 of the wire, high strain is observed which promotes the transition of LAGBs to HAGBs, leading to fragments of sub-grains and the occurrence of complete DRX in this region as depicted with small grain sizes. From TMAZ 1 to TMAZ 2 as parameter Z decreases to 14.5, corresponding to increase in grain size to 5.5 μm is captured. The spatial thermo-mechanical distribution in the workpiece and the extruded wire, show a clear correlation with the grain size and Z parameter. It is crucial to highlight that the type of DRX obtained, as defined by the Z parameter, may vary depending on alloying elements [40, 41] and stacking fault energies [42]. Overall, the applied sticking conditions lead to a fully refined microstructure, which agrees with observation in the literature [35]. However, in the current experiment illustrated in Fig. 5, a partially refined microstructure was observed within the wire. This indicates the occurrence of distinct friction condition, i.e. sliding, which is investigated in the following.

Material flow and microstructure zones due to sliding friction condition in FE

Figure 9 illustrates the spatial temperature and strain distribution obtained which aligns with the experimentally deduced microstructural zones in the workpiece. The maximum temperature obtained in the sliding friction condition is 41 °C higher than sticking condition. The temperature difference implies that in sliding friction condition the nodes of the die and workpiece slide against each other, hence the die rotation leads to more heat generation due to friction than material shearing. In Fig. 9(b), it is evident that the sliding friction condition results in less material shearing as depicted with a decrease in the maximum strain contribution to 16.5 compared to the strain of 28 reported in the sticking condition. In the extruded wire, the effects of sliding friction conditions are pronounced. In this context, an inhomogeneous strain distribution is observed and lack of sustained homogeneous plastic deformation in the wire. This inhomogeneous strain distribution results in the simultaneous introduction of TMAZ 1 and TMAZ 2 in the extruded wire.

Furthermore, with sliding friction condition, the strain distribution in TMAZ 1 and TMAZ 2 as inferred with the micrograph is correlated to the Z parameter and grain size calculated. Figure 9(c) and (d) show the spatial distribution of the Z parameter and grain size respectively on the workpiece, with characteristic inhomogeneous distribution in the extruded wire. Correspondingly in Fig. 9(c-d), the outer region TMAZ 1 of the extruded wire with high Z param-
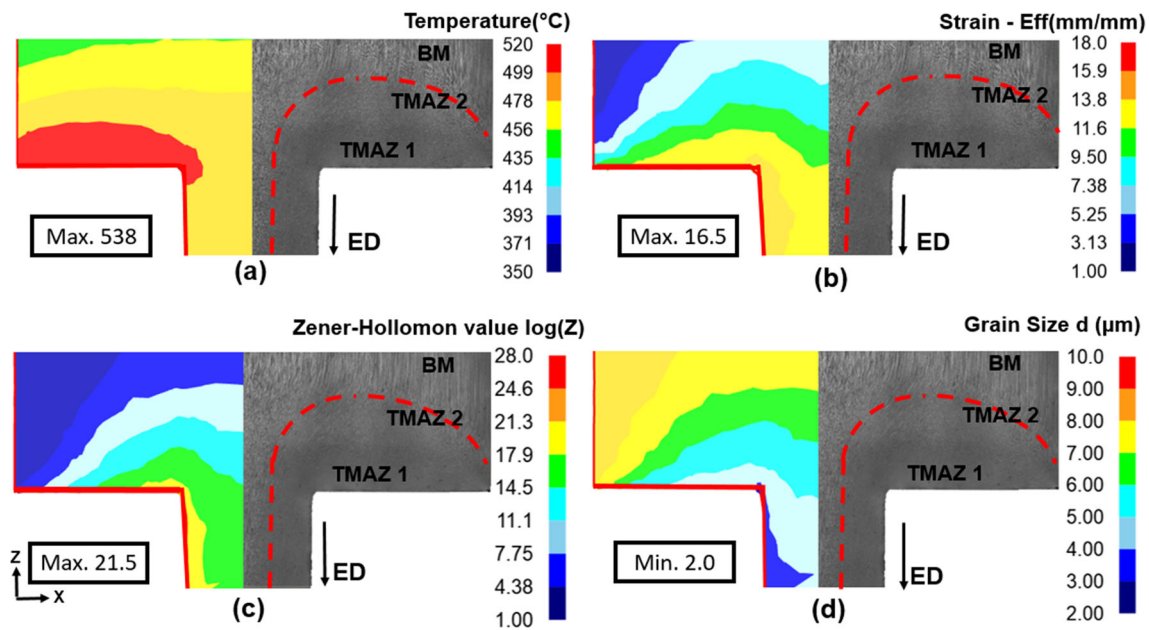
Fig. 9 Spatial distribution of (a) temperature; (b) strain; (c) Zener-Hollomon parameter; and (d) grain size in the workpiece with sliding friction condition applied at the die-workpiece interface in FE at $t^{process}$ = 50 s

eter and low grain size respectively, depicts DRX grains in the microstructure. On the other hand, the center region corresponding to TMAZ 2 of the extruded wire shows low Z parameter and high grain size, which is consistent with partially recrystallized grains in the microstructure. This observation suggests that the transition from sticking to sliding condition leads to a significant decrease in the degree of DRX and a shift towards microstructural inhomogeneity within the extruded wire.

Finally, significant material flow transition is observed within the microstructural zones formed in the workpiece due to sliding friction conditions. Figure 10(a) captures the material flow transition regions A and B in the velocity maps in the TMAZ 1 and 2 zones, respectively. Region A is the origin of the material flow and shows a diversion of the

material flow from BM to plasticized material in TMAZ 2 flowing towards the die orifice. The plasticized material in TMAZ 1 experiences another transition from a low to high material flow velocity as depicted by region B. This results from high frictional work occurring at the die edge, which is affirmed by high temperature and strain. Figure 10(b) shows the material flow pattern resulting from the flow behavior in different microstructural zones. The partially deformed pattern (straight lines) within region A corresponds to the BM while the deformed pattern (curved lines) depicts the TMAZ 2. The part of TMAZ 2 close to the die orifice as shown in Fig. 10(b) with a long flow pattern hints at elongated grains formed in the extrusion direction in the wire. This observation reveals the significance and interpretation of material flow behavior in the examined microstructural
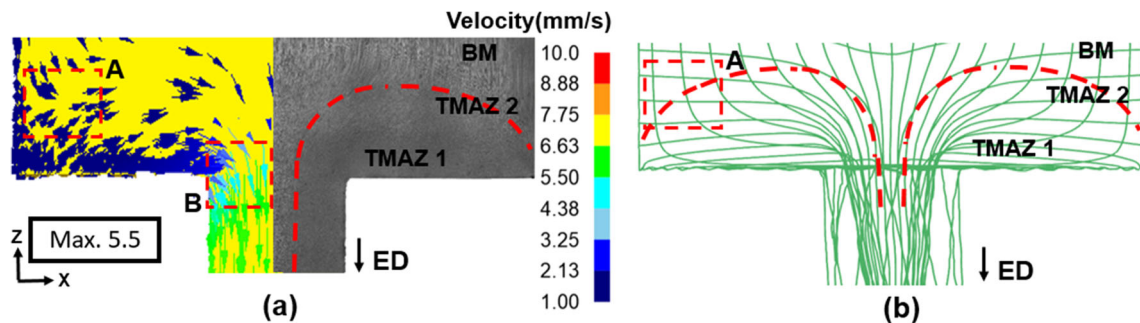
Fig. 10 Spatial distribution of material flow (a) velocity; and (b) pattern in the workpiece during FE with sliding friction condition at $t^{process}$ = 50 s, with region A showing a transition from BM to TMAZ 2

zones. Notably, the identified microstructure zones such as TMAZ 1, TMAZ 2, and BM correspond to heavy deformation zone (HDZ), shear zone (SZ), and deformation zone (DZ), respectively in CE [43] with unique characteristics due to additional aspect of rotation induced friction in FE.

Conclusion

In this work, FEM is presented for the extrusion processes of CE and FE respectively. Based on the results, the effect of rotation and different friction conditions lead to the following conclusions:

- The FEM accurately captures the process history, rotation, thermo-mechanical conditions, and friction conditions prevalent in extrusion.
- The additional aspect of die rotation in FE is instrumental in reducing the required process force compared to CE without pre-heating.
- The sticking condition in FE reveals the characteristic deformation mechanism through an in-plane shear leading to homogeneous grain refinement in the full extruded wire.
- The temperature and strain distribution validate the occurrence of CDRX as the dominant mechanism of refinement with a Z parameter of 28 and grain size around 2 - 3 μm in the TMAZ 1 in the case of sticking friction condition, which aligns well with the experimentally determined grain size.
- For sliding friction condition, inhomogeneous spatial strain distribution leads to inhomogeneous grain refinement across the extruded wire.
- A comparison between the sticking and sliding conditions indicates that transitioning from sticking to sliding conditions results in a decrease in the Z parameter and an increase in grain size.

Declarations

References

1. Ansari MA, Behnagh RA, Narvan M, Naeini ES, Givi MKB, Ding H (2001) Optimization of friction stir extrusion (fse) parameters through taguchi technique. Trans Indian Inst Metals 69:1351–1357. https://doi.org/10.1007/s12666-015-0686-6
2. Tang W, Reynolds A (2010) Production of wire via friction extrusion of aluminum alloy machining chips. J Mater Process Technol 210(15):2231–2237. http://www.sciencedirect.com/science/article/pii/S0924013610002463
3. Haghshenas M, Gerlich A (2018) Joining of automotive sheet materials by friction-based welding methods: A review. Eng Sci Technol Int J 21(1):130–148. https://www.sciencedirect.com/science/article/pii/S2215098617314921
4. Ghosh A (2001) Segregation in cast products. Sadhana 26:5–24. https://doi.org/10.1007/BF02728476
5. Li X, Tang W, Reynolds A, Tayon W, Brice C (2016) Strain and texture in friction extrusion of aluminum wire. J Mater Process Technol 229:191–198. https://www.sciencedirect.com/science/article/pii/S0924013615301199
6. Baffari D, Buffa G, Fratini L (2017) A numerical model for wire integrity prediction in friction stir extrusion of magnesium alloys. J Mater Process Technol 247:1–10. http://www.sciencedirect.com/science/article/pii/S0924013617301358
7. Li L, Reza-E-Rabby M, Overman N, Wang T, Whalen S, Grant G, Mathaudhu S, Soulami A (2022) Analysis of contact conditions and microstructure evolution in shear assisted processing and extrusion using smoothed particle hydrodynamics method. Mater Des 221:1–1111010. https://www.sciencedirect.com/science/article/pii/S0264127522006323
8. Tahmasbi K, Mahmoodi M (2018) Evaluation of microstructure and mechanical properties of aluminum aa7022 produced by friction stir extrusion. J Manuf Process 32:151–159. https://www.sciencedirect.com/science/article/pii/S1526612518300501
9. Halak RM, Rath L, Suhuddin UFHR, dos Santos JF, Klusemann B (2022) Changes in processing characteristics and microstructural

evolution during friction extrusion of aluminum. Int J Mater Form 15(24):1960–6214. https://doi.org/10.1007/s12289-022-01670-y

10. Li X, Reynolds AP, Baoqiang C, Jialuo D, Williams S (2016) in TMS 2015 144th Annual Meeting & Exhibition. Springer International Publishing, Cham, pp 445–452

11. Li G, Jinn J, Wu W, Oh S (2001) Recent development and applications of three-dimensional finite element modeling in bulk forming processes. J Mater Process Technol 113(1):40–45. http://www.sciencedirect.com/science/article/pii/S0924013601005908. 5th Asia Pacific conference on Materials processing

12. Parviz A, Givi B, Kazem M, Mostafa A (2015) Microstructural simulation of friction stir welding using a cellular automaton method: a microstructure prediction of AZ91 magnesium alloy. Int J Mech Mater Eng 10:1–20. https://doi.org/10.1186/s40712-015-0048-5

13. Janga VSR, Awang M, Yamin MF, Suhuddin UFH, Klusemann B, dos Santos JF (2021) Experimental and numerical analysis of refill friction stir spot welding of thin AA7075-T6 sheets. Materials 14:1–23. https://www.sciencedirect.com/science/article/pii/S0261306915001594

14. Chu Q, Yang X, Li W, Vairis A, Wang W (2018) Numerical analysis of material flow in the probeless friction stir spot welding based on coupled eulerian-lagrangian approach. J Manuf Process 36:181–187. https://doi.org/10.1016/j.jmapro.2018.10.013. https://www.sciencedirect.com/science/article/pii/S1526612518310429

15. Assidi M, Fourment L, Guerdoux S, Nelson T (2010) Friction model for friction stir welding process simulation: Calibrations from welding experiments. Int J Mach Tools Manuf 50(2):143–155. https://www.sciencedirect.com/science/article/pii/S0890695509002363

16. Behnagh RA, Shen N, Ansari MA, Narvan M, Besharati Givi MK, Ding H (2016) Experimental analysis and microstructure modeling of friction stir extrusion of magnesium chips. J Manuf Sci Eng 138(4):041008

17. Hassanamraji N, Eivani AR, Aboutalebi MR (2021) Finite element simulation of deformation and heat transfer during friction stir processing of as-cast AZ91 magnesium alloy. J Mater Res Technol 14:2998–3017. https://www.sciencedirect.com/science/article/pii/S2238785421009157

18. Jain R, Pal SK, Singh SB (2016) A study on the variation of forces and temperature in a friction stir welding process: A finite element approach. J Manuf Process 23:278–286. http://www.sciencedirect.com/science/article/pii/S1526612516300251

19. Rath L, Suhuddin UF, Klusemann B (2022) Comparison of friction extrusion processing from bulk and chips of aluminum-copper alloys. Key Eng Mater 926:471–480. https://doi.org/10.4028/p-vw04z5

20. Chen G, Zhang S, Zhu Y, Yang C, Shi Q (2019) Thermo-mechanical analysis of friction stir welding: a review on recent advances. Acta Metall Sin (English Letters). https://doi.org/10.1007/s40195-019-00942-y

21. Bodunrin MO (2020) Flow stress prediction using hyperbolic-sine arrhenius constants optimised by simple generalised reduced gradient refinement. J Mater Res Technol 9(2):2376–2386. https://www.sciencedirect.com/science/article/pii/S2238785419315005

22. Asadi P, Mahdavinejad R, Tutunchilar S (2011) Simulation and experimental investigation of FSP of AZ91 magnesium alloy. Mater Sci Eng A 528(21):6469–6477. https://www.sciencedirect.com/science/article/pii/S0921509311005843

23. Shen Z, Ding Y, Gerlich AP (2020) Advances in friction stir spot welding. Crit Rev Solid State Mater Sci 45(6):457–534. https://doi.org/10.1080/10408436.2019.1671799

24. Rokni M, Zarei-Hanzaki A, Roostaei AA, Abolhasani A (2011) Constitutive base analysis of a 7075 aluminum alloy during hot compression testing. Mater Des 32(10):4955–4960. http://www.sciencedirect.com/science/article/pii/S0261306911003918

25. Trimble D, O'Donnell G (2015) Constitutive modelling for elevated temperature flow behaviour of AA7075. Mater Des 76:150–168. https://www.sciencedirect.com/science/article/pii/S0261306915001594

26. Andrzej K, Tomasz T (2020) A fully coupled thermo-mechanical numerical modelling of the refill friction stir spot welding process in alclad 7075–T6 aluminium alloy sheets. Arch Civ Mech Eng 20(117):1644–9665. https://doi.org/10.1007/s43452-020-00127-w

27. Kobayashi S, Oh SI, Altan T (1989) Metal forming and the finite-element method (Oxford university press)

28. Buffa G, Hua J, Shivpuri R, Fratini L (2006) A continuum based fem model for friction stir welding-model development. Mater Sci Eng A 419(1):389–396. http://www.sciencedirect.com/science/article/pii/S0921509305011354

29. Liu Q, Li W, Zhu L, Gao Y, Xing L, Duan Y, Ke L (2022) Temperature-dependent friction coefficient and its effect on modeling friction stir welding for aluminum alloys. J Manuf Process 84:1054–1063. https://www.sciencedirect.com/science/article/pii/S1526612522007617

30. Yang C, Dai Q, Shi Q, Wu C, Zhang H, Chen G (2022) Flow-coupled thermo-mechanical analysis of frictional behaviors at the tool-workpiece interface during friction stir welding. J Manuf Process 79:394–404. https://www.sciencedirect.com/science/article/pii/S1526612522003103

31. Mei RB, Du Y, Bao L, Zhang X, Zhang B, Zhou Z (2015) Study on hot deformation behavior of 7085 aluminum alloy during backward extrusion process. Model Simul Eng 2015:1–8. https://doi.org/10.1155/2015/514863

32. Ezatpour H, Haddad Sabzevar M, Sajjadi S, Huang Y (2014) Investigation of work softening mechanisms and texture in a hot deformed 6061 aluminum alloy at high temperature. Mater Sci Eng A 606:240–247. https://www.sciencedirect.com/science/article/pii/S0921509314003682

33. Humphreys F, Hatherly M (2004) Hot deformation and dynamic restoration. Recrystallization and related annealing phenomena pp 415–450

34. Baffari D, Buffa G, Campanella D, Fratini L, Reynolds AP (2017) Process mechanics in friction stir extrusion of magnesium alloys chips through experiments and numerical simulation. J Manuf Process 29:41–49. https://www.sciencedirect.com/science/article/pii/S1526612517301743

35. Suhuddin UF, Rath L, Halak RM, Klusemann B (2023) Microstructure evolution and texture development during production of homogeneous fine-grained aluminum wire by friction extrusion. Materials Characterization p. 113252 . https://www.sciencedirect.com/science/article/pii/S1044580323006113

36. Wang X, Gao Y, Liu X, McDonnell M, Feng Z (2021) Tool-workpiece stick-slip conditions and their effects on torque and heat generation rate in the friction stir welding. Acta Mater 213:1–116969. https://www.sciencedirect.com/science/article/pii/S1359645421003499

37. McNelley T, Swaminathan S, Su J (2008) Recrystallization mechanisms during friction stir welding/processing of aluminum alloys. Scr Mater 58(5):349–354. https://www.sciencedirect.com/science/article/pii/S1359646207007464

38. Cerri E, Evangelista E, Forcellese A, McQueen H (1995) Comparative hot workability of 7012 and 7075 alloys after different pretreatments. Mater Sci Eng A 197(2):181–198. https://www.sciencedirect.com/science/article/pii/0921509394097143

39. Sun Y, Pan Q, Huang Z, Wang W, Wang X, Li M, Lai J (2018) Evolutions of diffusion activation energy and zener-hollomon parameter of ultra-high strength Al-Zn-Mg-Cu-Zr alloy during hot compression. Prog Nat Sci Mater Int 28(5):635–646. https://www.sciencedirect.com/science/article/pii/S1002007118302235

40. Wang X, Xiao D, Wu M, Liu W (2021) Deformation behavior and microstructure evolution of Al-5.06Mg-1.67Li-0.51Zn alloy under hot compression. J Mater Res Technol 15:4516–4528. https://www.sciencedirect.com/science/article/pii/S2238785421012205

41. Yu Y, Pan Q, Wang W, Huang Z, Xiang S, Liu B (2021) Dynamic softening mechanisms and zener-hollomon parameter of Al-Mg-Si-Ce-B alloy during hot deformation. J Mater Res Technol 15:6395–6403. https://www.sciencedirect.com/science/article/pii/S2238785421013600

42. Sakai T, Belyakov A, Kaibyshev R, Miura H, Jonas JJ (2014) Dynamic and post-dynamic recrystallization under hot, cold and severe plastic deformation conditions. Prog Mater Sci 60:130–207. https://www.sciencedirect.com/science/article/pii/S0079642513000698

43. Yu H, Park SH, You BS (2015) Die angle dependency of microstructural inhomogeneity in an indirect-extruded AZ31 magnesium alloy. J Mater Process Technol 224:181–188. http://www.sciencedirect.com/science/article/pii/S0924013615002034